Bioinspiration &
Biomimetics

PAPER

A bio-inspired study on tidal energy extraction with flexible flapping wings

To cite this article: Wendi Liu *et al* 2013 *Bioinspir. Biomim.* **8** 036011

Bioinspir. Biomim. **8** (2013) 036011 (16pp) doi:10.1088/1748-3182/8/3/036011

A bio-inspired study on tidal energy extraction with flexible flapping wings

Wendi Liu[1], **Qing Xiao**[1,3] **and Fai Cheng**[2]

[1] Department of Naval Architecture and Marine Engineering University of Strathclyde, Glasgow, G4 0LZ, UK
[2] Strategic Research Group, Lloyd's Register Group Limited 71 Fenchurch Street, London, EC3M 4BS, UK

E-mail: qing.xiao@strath.ac.uk

Received 27 June 2013
Accepted for publication 17 July 2013
Published 27 August 2013
Online at stacks.iop.org/BB/8/036011

Abstract
Previous research on the flexible structure of flapping wings has shown an improved propulsion performance in comparison to rigid wings. However, not much is known about this function in terms of power efficiency modification for flapping wing energy devices. In order to study the role of the flexible wing deformation in the hydrodynamics of flapping wing energy devices, we computationally model the two-dimensional flexible single and twin flapping wings in operation under the energy extraction conditions with a large Reynolds number of 10^6. The flexible motion for the present study is predetermined based on *a priori* structural result which is different from a passive flexibility solution. Four different models are investigated with additional potential local distortions near the leading and trailing edges. Our simulation results show that the flexible structure of a wing is beneficial to enhance power efficiency by increasing the peaks of lift force over a flapping cycle, and tuning the phase shift between force and velocity to a favourable trend. Moreover, the impact of wing flexibility on efficiency is more profound at a low nominal effective angle of attack (AoA). At a typical flapping frequency $f^* = 0.15$ and nominal effective AoA of 10°, a flexible integrated wing generates 7.68% higher efficiency than a rigid wing. An even higher increase, around six times that of a rigid wing, is achievable if the nominal effective AoA is reduced to zero degrees at feathering condition. This is very attractive for a semi-actuated flapping energy system, where energy input is needed to activate the pitching motion. The results from our dual-wing study found that a parallel twin-wing device can produce more power compared to a single wing due to the strong flow interaction between the two wings.

(Some figures may appear in colour only in the online journal)

Nomenclature

A	sweep area (m^2)
c	chord length (m)
$C_l(t)$	instantaneous lift coefficient
$C_m(t)$	instantaneous moment coefficient
C_{op}	power coefficient
d_b	foil displacement at trailing edge (m)
f	frequency of flapping wing (Hz)
f^*	reduced frequency
$h(t)$	instantaneous heaving position (m)
h_0	amplitude of heaving motion (m)
l_c	pitching centre (m)
p	instantaneous power (W)
S_f	gap ratio between twin wings
t	instant time (s)
T	oscillating period (s)
U_∞	free-stream velocity (m/s)
x_f	x coordinate in body-fixed system (m)
$y(x_f, t)$	instantaneous foil lateral excursion

[3] Author to whom any correspondence should be addressed.

α_0	nominal effective AoA (deg)
$\alpha_{\text{eff}}(t)$	effective angle of attack (deg)
$\alpha_f(t)$	local AoA at the leading edge in body-fixed coordinate system (deg)
$\alpha_l(t,x)$	local effective AoA (deg)
$\alpha_t(x_f)$	lateral amplitude
η	energy extraction efficiency
θ_0	amplitude of pitching motion (deg)
$\theta_l(t,x)$	local pitching angle (deg)
θ_{l0}	averaged local pitching amplitude (deg)
$\theta_t(t)$	instantaneous pitching angle (deg)
ω	angular frequency
AoA	angle of attack
LEC	leading edge control (model)
LEV	leading edge vortex
TEC	trailing edge control (model)
LE	leading edge
FSI	fluid–structure interaction

1. Introduction

Biomimetics is the study of the mechanisms evolved in nature's biological system and utilizing them for various applications. Over the past ten years, research studies on the aerodynamics/hydrodynamics of biomimetics have been carried out rapidly due to the increasing demand from the aero/marine industry and the defence sector. One interesting phenomenon in the area that is relevant to animal propulsion and manoeuvrability features is the wing flapping motion, which is defined as an integrated motion from a rotated pitch motion with an up and down heave motion. Typical examples include insect wings in a hovering mode and subcarangiform fish caudal/tail fins in a propelling and manoeuvring mode. The study on the flapping wing aerodynamics/hydrodynamics has already been widely applied in the design of engineering devices, such as micro aerial vehicle (MAV), autonomous underwater vehicles (AUV) and robotic fish (Sfakiotakis *et al* 1999, Triantafyllou *et al* 2004, Liu 2005, Fish and Lauder 2006).

In recent years there has been a growing demand to exploit the new types of available ocean renewable devices. As a result, the flapping or oscillating wing has further extended its application from just the propulsion/manoeuvring aspect (energy consumption) to the energy harvesting area (McKinney and DeLaurier 1981, Jones and Platzer 1997, Jones *et al* 2003, Kinsey and Duman 2008, 2012a, 2012b, Zhu and Peng 2009, Zhu *et al* 2009, Zhu 2011, Xiao *et al* 2012). Investigations from relevant research studies show that a flapping motion can vary from its propulsion mode to its energy extraction mode if the wing pitches at an angle exceeding its heave induced angle of attack (AoA). The power efficiency generated is comparable to a conventional tidal turbine with rotational blades. The recent research study of Xiao *et al* (2012) also revealed that an appropriately proposed non-sinusoidal pitch trajectory can effectively enhance device efficiency via tuning the instantaneous AoA to a favourable profile. A series of work has been conducted by Kinsey and Dumas (2008, 2012a, 2012b) on the flapping wing device through experiment and simulation. Recent work on a three-dimensional wing aimed to access the influence of wing span-length on power generation. With a given aspect ratio AR of 5.0, their prediction was comparable to their experiment data. Efforts were also devoted to analysing the dual flapping wing device in a tandem arrangement under the condition of high incoming Reynolds number at 5×10^5. An optimized gap (L) between upstream and downstream foil was found to be at a value of L/c of 5.4 to achieve optimal efficiency.

Currently, existing work mainly focuses on the investigation of a rigid wing, which is only sensible under the normal weather and sea conditions, where the deformation of a wing blade can be ignored. However, under some extreme flow conditions, a large-scale blade may experience a huge unsteady loading, resulting in a potential blade deformation in chord-wise and span-wise directions. Studies that are restricted to rigid blades have severe limitations in their practical application.

In nature, insect wings and fish fins are complicated flexible structures that can deform passively, although there are obvious distinctions between them. Previous studies on the flexible role of insect wings, such as those of a butterfly, hawkmoth or bee, conducted on the propulsion performance, suggested that some degree of flexibility can achieve a higher level of aerodynamics propulsive thrust by manipulating the leading edge vortex (LEV) enhancement/decay mechanism. In particular, the bending and twisting motion of a flexible wing can effectively vary its flying direction and generate asymmetric forces between the upstroke and downstroke motion, leading to a large cycle-averaged aerodynamics force (Wootton 1990, Zhu 2007, Nakata and Liu 2012). Combes and Daniel (2003a, 2003b) conducted a relevant study on evaluating the impact of wing stiffness variation in a chord-/span-wise direction on the wing distortion and produced lifting. Their measurements of flexure stiffness and wing venation pattern in the forewings of 16 insect species found that the stiffness in the span-wise direction was approximately one- or two-orders magnitude higher than that in the chord-wise direction. A sharply decayed flexural stiffness was observed from the wing base to the leading edge (LE). The maximum displacement was less than 0.08 and 0.15 in span-wise and chord-wise, respectively. Zhu (2007) performed a computational study of a wing with span-wise and chord-wise distortion, in an attempt to assess the function of wing flexure on propulsion performance in high- and low-density fluid environments. They found that the inertia of a flexible wing played a major role in wing deformation if the wing was immersed in a low-density fluid surrounding, such as air. Both thrust and propulsion efficiency reduced with increasing flexure motion. However, within a high-density surrounding, like water, the external fluid loading has a primary impact on wing deformation compared with the wing internal inertial force. With their simulation results, the chord-wise flexibility was proved to increase wing propulsion efficiency. These findings highlight the significance of the flexible structure deformation in promoting aerial animals' propulsion movement. We will also find out if it plays a similar role in operating the ocean energy device that we are about to introduce.

It has always been accepted that the biological flexible structure of fish fins plays an important role in fish propulsion and manoeuvring. A recent study by Shoele and Zhu (2012) addressed the flexibility impact of trout ray fins on trout propelling. With the use of the fully coupled fluid–structure interaction (FSI) model, numerical prediction by Shoele and Zhu tested a series of cases to study the relationship between the thrust and fluid field feature. By comparing it with the rigid ray fin model, the flexible models could enhance the thrust significantly. By controlling the LE stiffness, i.e. strengthening the LE, the propulsion efficiency could reach a higher value. Some degree of domination at the LE could effectively increase local AoA, and thus affect the forming and shedding of the LEV. An enhanced hydrodynamic force would be generated if the local AoA at the LE was around 30°.

Inspired by the advantages of a flexible wing over a rigid wing in flapping propulsion, this study investigates whether the flexible structure influence is also beneficial to a flapping wing energy device. To the best of the authors' knowledge, no relevant work has been performed in this area, although a small number of studies have been done on the potential distortion of a wind turbine blade under extreme high wind speed conditions (Lachenal *et al* 2012, Turnock *et al* 2009). To this end, we will begin our investigation by comparing the power efficiency of two flexible models, emulating the hawkmoth wing (trailing edge control (TEC)) and the trout ray fin (leading edge control (LEC)) model against that of a rigid wing. Subsequently, we seek to develop a new preferred wing using the insights gained from the above two models. Since the simulation will be based on a two-dimensional simulation model, only chord-wise flexibility will be taken into account. At this stage, we will use *a priori* structural result that will determine our prescribed wing deformation, which means our computational fluid dynamic (CFD) study is decoupled from structural analysis. Although we cannot disregard the limitations of the approaches in the present study, in particular the critical features of the three-dimensional flapping wing with passive flexible deformation, nonetheless the research is taking the lead in exploring the field of problems with increasing intricacy. Apart from a single flexible wing study, the present study will further include a flexible twin-wing system mimicking the fish swimming in schools and the birds flying in flocks to preserve their flow energy between neighbours.

The outline of the rest of the paper is as follows. We begin by describing the problem with relevant flexible models and parameters that control the flapping wing kinematics and power generation features along with the governing equations and numerical methods in section 2. In this section we also demonstrate the validity of the developed numerical methods in modelling such flows. In section 3, a systematic presentation of the predicted results is included. We start with an examination of the efficiency of the flexible wing enhancing device via a detailed analysis in the wake structure and various instantaneous parameters and local effective AoA, followed by a discussion of the results with a systematic parametric study that is pertinent to global and local flexibility. Unlike the other existing works of Kinsey and Dumas (2008, 2012a, 2012b), our particular interest is focused on the flexible wing's influence by comparing the rigid and flexible data in a turbulence flow regime to emphasize the distinction between them.

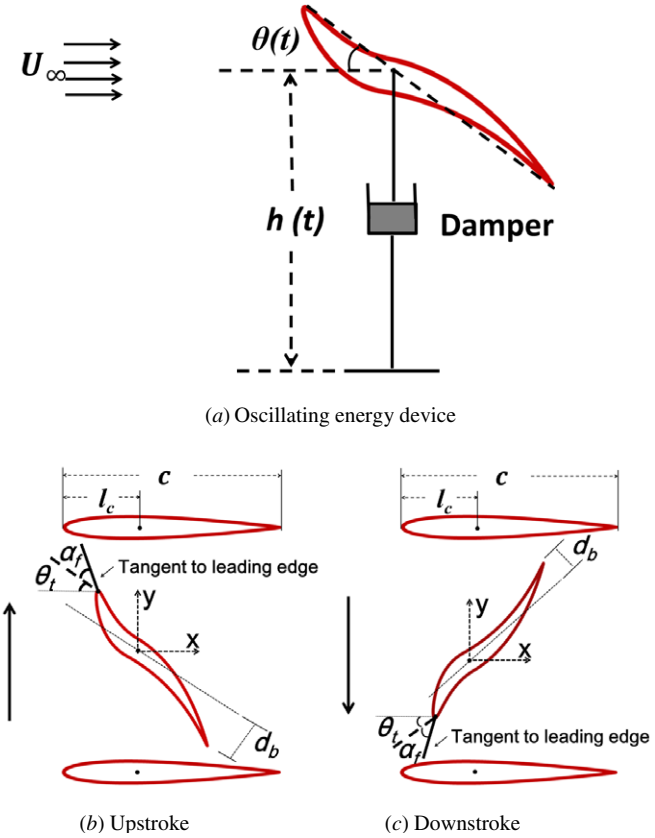

(*a*) Oscillating energy device

(*b*) Upstroke (*c*) Downstroke

Figure 1. Schematic diagram for (*a*) oscillating energy device, (*b*) upstroke and (*c*) downstroke.

2. Problem description and methodology

2.1. Problem description

The configuration of the current problem is shown in figure 1, where an oscillating NACA0012 hydrofoil is immersed in a uniform viscous water flow. Practically, the device is forced to pitch/rotate at a fixed axis, so the generated unsteady hydrodynamic force around the foil and water surrounding it activates the foils up and down heave motion. The kinematic energy of the water current is converted to the mechanical energy associated with the heave motion via a damper, and then transformed to electricity by a generator.

To simplify the problem, most existing work assumes that both the pitch and heave motion are predetermined, and thus the power estimated is solely the available hydrodynamic power, ignoring the actuating mechanism in the system (McKinney and DeLaurier 1981, Jones and Platzer 1997, Jones *et al* 2003, Kinsey and Dumas 2008, 2012a, 2012b, Xiao *et al* 2012). In this context, the energy extraction is obtained through a foil undergoing a combined pitch and heave motion with the following specified equations:

$$h(t) = h_0 \sin(\omega t), \tag{1}$$

$$\theta_t(t) = \theta_0 \sin\left(\omega t - \frac{\pi}{2}\right), \tag{2}$$

where h_0 and θ_0 are the amplitude of heave and pitch, respectively. In the present study, the foil pitches at $l_c = 1/3$ chord length from its LE.

To examine the bio-inspired animal flexible structure impact on the oscillating wing device's performance, the flexible deformation of foil is specified as a function of instantaneous time, wing chord-length and flapping frequency. The instantaneous lateral excursion of the foil (y (x_f, t)) is defined as based on a body-fixed coordinate system:

$$y(x_f, t) = \alpha_t(x_f)\sin\left(\omega t - \frac{\pi}{2}\right), \tag{3}$$

where x_f is the local coordinate of foil relative to the pitching axis, $a_t(x_f)$ is the lateral amplitude defined as a piecewise function as

$$\alpha_t(x_f) = \begin{cases} -l_c * \left(\dfrac{x_f}{l_c}\right)^n * \sin\alpha_f(t) & x_f < 0 \\ (c - l_c) * \left(\dfrac{x_f}{c - l_c}\right)^n * d_b & x_f \geqslant 0 \end{cases}, \tag{4}$$

where α_f is the local angle of attack near the leading edge in a body-fixed coordinate system and d_b is the foil displacement at the trailing edge, as shown in figures 1(*b*) and (*c*).

The following four different wing models are studied depending on their specific flexible motion.

(a) *Rigid model* ($\alpha_f = 0^\circ$, $d_b/c = 0$). This is a conventional model that is utilized by the oscillating wing device. It is commonly used in industrial application and relevant research. Here it is used as a benchmark case to evaluate the device's capability in comparison to other flexible wings. By switching off the flexible motion (i.e. setting $\alpha_f = 0^\circ$and $d_b/c = 0$), the motion equation is simplified to

$$\begin{aligned} h(t) &= h_0 \sin(\omega t); \\ \theta_t(t) &= \theta_0 \sin\left(\omega t - \frac{\pi}{2}\right); \\ y(x_f, t) &= 0; \end{aligned} \tag{5}$$

(b) *Leading edge control (LEC) model* ($\alpha_f \neq 0^\circ$, $d_b/c = 0$). This imitates the ray fin of a rainbow trout, as shown in figures 2(*a*) and (*c*). Rainbow trout use their undulating ray fin as an auxiliary thrust producer. The fin-rays are connected by a flexible membrane that is external to the thrust body and joined with the trout's back muscles internally so that the locomotion and stiffness of each fin-ray can be actively controlled by the trout (Sfakiotakis *et al* 1999). A previous study by Shoele and Zhu (2012) showed that trout propels itself by flapping its flexible fin at a relative *low* frequency. The active control of the stiffness (strengthen) at the fin LE generated a large thrust force which is attributed to the LEV shedding. Shoele and Zhu's research shows significant influence of the LE feature on the LEV. Efficient domination of the LE feature could achieve the goal of manipulating the LEV. To apply this biomimetic concept to the oscillating wing energy device, we vary the local AoA (α_f) at the LE from 7.5° to 30°, using the suggestions from Shoele and Zhu (2012). With $d_b/c = 0$, the motion profile becomes

$$\begin{aligned} h(t) &= h_0 \sin(\omega t); \\ \theta_t(t) &= \theta_0 \sin\left(\omega t - \frac{\pi}{2}\right); \\ y(x_f, t) &= \alpha_0(x_f) \sin\left(\omega t - \frac{\pi}{2}\right); \\ \alpha_t(x_f) &= \begin{cases} -l_c * \left(\dfrac{x_f}{l_c}\right)^n * \sin\alpha_f(t); & x_f < 0 \\ 0; & x_f \geqslant 0 \end{cases} \end{aligned} \tag{6}$$

(c) *Trailing edge control (TEC) model* ($\alpha_f = 0^\circ$, $d_b/c \neq 0$). The model is inspired by the flapping insect wing, particularly the hawkmoth wing shown in figures 2(*b*) and (*d*). A numerical investigation by Nakata and Liu (2012) and experiments from Combes and Daniel (2003a, 2003b) indicated that the hawkmoth wing has the lowest stiffness at its trailing edge and deforms profoundly when the wing flaps at *high* frequency, where a large loading is produced. To represent the foil flexible effect associated with the hawkmoth wing, the trailing edge deformation (d_b/c) is varied from 0.05 to 0.15, as recommended by Combes and Daniel (2003a, 2003b). The motion equation is thus written as

$$\begin{aligned} h(t) &= h_0 \sin(\omega t); \\ \theta_t(t) &= \theta_0 \sin\left(\omega t - \frac{\pi}{2}\right); \\ y(x_f, t) &= \alpha_0(x_f) \sin\left(\omega t - \frac{\pi}{2}\right); \\ \alpha_t(x_f) &= \begin{cases} 0; & x_f < 0 \\ (c - l_c) * \left(\dfrac{x_f}{c - l_c}\right)^n * d_b; & x_f \geqslant 0 \end{cases} \end{aligned} \tag{7}$$

(d) *Integrated model* ($\alpha_f \neq 0^\circ$, $d_b/c \neq 0$). The new concept proposed here is initiated by combining the propulsion enhancement benefits from LEC at a low flapping frequency with the TEC at high frequency. Since both α_f at LE and displacement d_b/c at trailing edge are not zero, the description of the overall motion equations are equations (1) to (4).

The snapshots of the above four models are plotted in figure 3 over one flapping cycle. The detailed parameter matrix in the present study is summarized in table 1. The heave amplitude (h_0/c) is given as 0.5 and 1.0, which are the widely adopted parameters in industry and research.

Flexible coefficient (n), the index in lateral amplitude equation (equation (4)), is a means to quantify the flexibility or flexural stiffness of wing material. Obviously, a large n represents a more flexible structure in the chord-wise direction. To quantify a localized deformation in the proximity of leading and trailing edges, two additional parameters are introduced, i.e. local LE AoA (α_f) and trailing edge displacement (d_b/c).

The flapping reduced frequency f^* is defined as

$$f^* = \frac{f * c}{U_\infty}, \tag{8}$$

where f is the frequency of the oscillating wing and U_∞ is the freestream velocity. The study by Kinsey and Dumas (2008) revealed that the optimal range of high efficiency existed between $f^* \approx 0.12$ and 0.18. Taking into account a moderate scale of device size, water current velocity (4 m s^{-1} in maximum), the oscillating reduced frequency in the present study varies from 0.05 to 0.25.

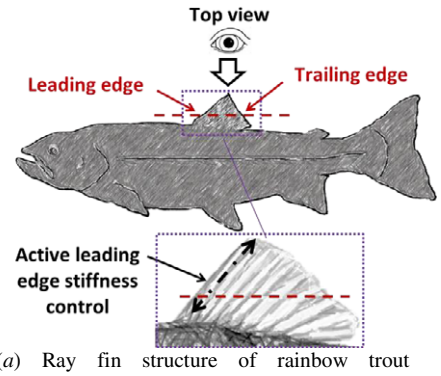

(*a*) Ray fin structure of rainbow trout (*Oncorhynchus mykiss*)

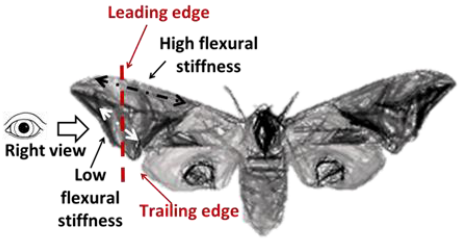

(*b*) Wing structure of hawkmoth (*Agrius Convolvuli)*

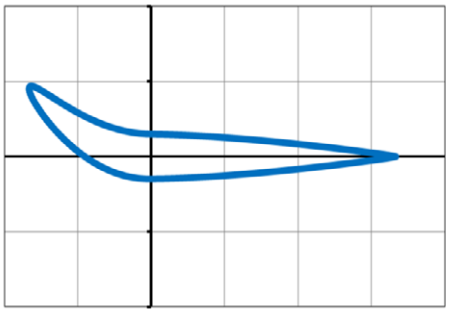

(*c*) Two-dimensional model of leading edge control model (top view)

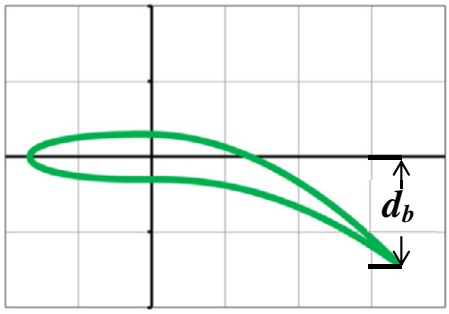

(*d*) Two-dimensional model of trailing edge control model (right view)

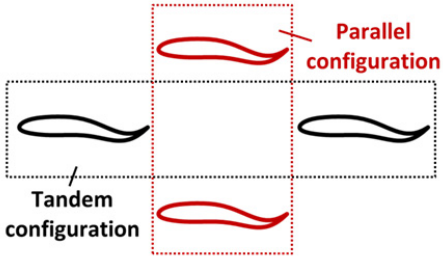

(*e*) Schematic illustrating fish swimming in group

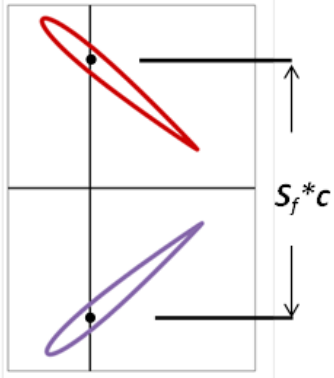

(*f*) Two-dimensional twin-wing parallel configuration

Figure 2. Structure of (*a*) rainbow trout fin, (*b*) hawkmoth wing, (*c*) two-dimensional model of leading edge control model (top view from (*a*)), (*d*) two-dimensional model of trailing edge control model (right view from (*b*)), (*e*) schematic illustrating fish swimming in group, (*f*) two-dimensional twin-wing parallel configuration.

Table 1. Various parameters investigated in the present study.

Type	Number of wing	Heave amplitude (h_0/c)	Flexible coefficient (n)	Leading edge local AoA (α_f)	Trailing edge displacement (d_b/c)	Maximum (nominal) effective AoA (α_0)	Pitch axis (x_f/c)	Twin-wing gap ratio (S_f)	Reduced frequency (f^*)
Rigid	1	0.5, 1.0	1	0°	0	0°, 5°, 10°	1/3	–	0.05–0.25
LEC	1	0.5	2, 3, 4	7.5°, 15°, 30°	0	10°	1/3	–	0.05–0.25
TEC	1	0.5	2, 5, 15	0°	0.05, 0.07, 0.15	10°	1/3	–	0.05–0.25
Integrated	1	0.5	Leading edge 3 Trailing edge 5	30°	0.15	0°, 5°, 10°	1/3	–	0.05–0.25
Rigid	2	0.5	1	0°	0	0°, 5°, 10°	1/3	2, 3	0.05–0.25
TEC	2	0.5	5	0°	0.05	0°, 5°, 10°	1/3	3	0.05–0.25

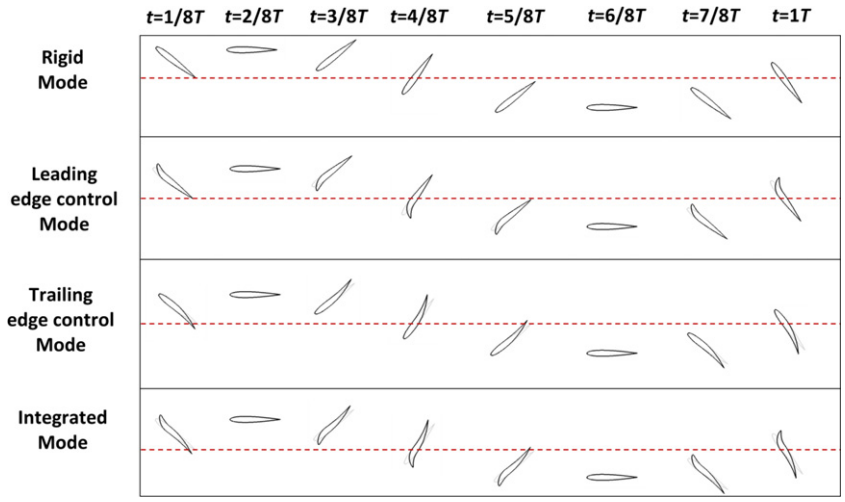

Figure 3. Snapshots for four models over one flapping cycle.

Apart from the above four single flexible/rigid models, attention is also focused on the twin-wing oscillating device, which is inspired by a group of flying or swimming animals to utilize energy extraction from the vortex interaction between them (Liao 2007) (figures 2(*e*) and (*f*)). Although this biomimetic concept has been widely studied in terms of propulsion dominant flow, investigation into the field of energy extraction is limited. The current research will focus on the parallel twin-wing configuration for both rigid and TEC models and the interaction between two wings will be studied. The description of the kinematic motions of twin wings is presented as

$$\boldsymbol{Foil1}: \begin{cases} h(t) = h_0 \sin(\omega t + \pi) + \dfrac{S_f * c}{2}; \\ \theta_t(t) = \theta_0 \sin\left(\omega t - \dfrac{3\pi}{2}\right); \\ y(x_f, t) = \alpha_0 (x_f \sin\left(\omega t - \dfrac{3\pi}{2}\right); \\ \alpha_t(x_f) = \begin{cases} 0; & x_f < 0 \\ (c - l_c) * \left(\dfrac{x_f}{c - l_c}\right)^n * d_b; & x_f \geqslant 0 \end{cases} \end{cases} \tag{9}$$

$$\boldsymbol{Foil2}: \begin{cases} h(t) = h_0 \sin(\omega t) - \dfrac{S_f * c}{2}; \\ \theta_t(t) = \theta_0 \sin\left(\omega t - \dfrac{\pi}{2}\right); \\ y(x_f, t) = \alpha_0 (x_f) \sin\left(\omega t - \dfrac{\pi}{2}\right); \\ \alpha_t(x_f) = \begin{cases} 0; & x_f < 0 \\ (c - l_c) * \left(\dfrac{x_f}{c - l_c}\right)^n * d_b; & x_f \geqslant 0 \end{cases} \end{cases} \tag{10}$$

As we can see, these two wings perform an anti-phase heave and pitch motion. Given the average gap ratio S_f of 2.0, defined as the vertical gap between two wings divided by chord length as shown in figure 2(*f*), the actual distance between two wings is 1.0c and 3.0c when they reach the nearest and distant positions, respectively.

With a flapping wing problem, one of the most important kinematic parameters is the effective AoA, which is determined by a blended impact from the wing pitch and heave motion. This is defined as

$$a_{\text{eff}}(t) = \theta_t(t) - \arctan\left(\frac{h(t)}{U_\infty}\right). \tag{11}$$

The maximum effective AoA, which is also sometimes called nominal effective AoA (α_0), is the maximum pitch angle a wing can reach during each cycle, i.e. $\theta_t(t) = \theta_0$, therefore,

$$\alpha_0 = \theta_0 - \arctan\left(\frac{\omega h_0}{U_\infty}\right). \tag{12}$$

Previous research shows that relying on the sign of α_0, a flapping wing can either work in an energy consumption regime as a propeller ($\alpha_0 < 0$) or in an energy extraction regime as an oscillating wing energy device ($\alpha_0 > 0$). A mutual stable status is reached when α_0 is equal to zero, which is normally called feathering state (Anderson *et al* 1998, Zhu 2011, Kinsey and Dumas 2008). One of the objectives of the current research is to examine whether an oscillating flexible wing could diminish its pitching amplitude at a feathering status (the nominal effective AoA boundary between the propulsion mode and energy extraction mode) relative to a rigid wing. With this success, the energy input to drive the pitching motion can be significantly reduced.

Aside from the above nominal effective AoA, in order to account for both the wing's chord-wise local flexure effect and the pitch angle, we define an equivalent local effective AoA as

$$a_l(t, x) = \theta_l(t, x) - \arctan\left(\frac{h(t)}{U_\infty}\right), \tag{13}$$

where $\theta_l(t, x)$ is a local pitch angle, defined as the angle of the local tangential line relative to a global x coordinate.

The non-dimensional instantaneous power coefficient C_{op} is determined by

$$C_{op} = \frac{p}{\frac{1}{2}\rho U_\infty^3 c} = \frac{1}{U_\infty^3}\left[C_l(t)\frac{\mathrm{d}h(t)}{\mathrm{d}t} + C_m(t)\frac{\mathrm{d}\theta(t)}{\mathrm{d}t}\right], \tag{14}$$

where $C_l(t)$ and $C_m(t)$ are the instantaneous lift moment coefficient, respectively, and p is the instantaneous power.

The total energy extraction efficiency η is defined as

$$\eta = \frac{\bar{p}}{\frac{1}{2}\rho U_\infty^3 c} = C_{op}\frac{c}{A}, \tag{15}$$

where A is the sweep area of the oscillating wing.

2.2. Numerical approach

Oscillating NACA0012 foils surrounded by time-dependent turbulent viscous flow are simulated according to the energy extraction purpose. The simulation is performed by solving the compressible unsteady Navier–Stokes equations at a low Mach number. The Reynolds number (Re) based on the far-stream velocity (U_∞) and chord-length (c) is $Re = 10^6$ and the k-ω two-equation turbulence model is used for turbulent modelling.

Given a control volume Ω with boundary surface S, the Reynolds-averaged governing equations for an unsteady turbulence flow using two-equation k-ω models are as follows:

$$\frac{\partial}{\partial t}\int_\Omega \boldsymbol{W}\,\mathrm{d}\Omega + \oint_{\partial\Omega}(\boldsymbol{F}_c - \boldsymbol{F}_d)\,\mathrm{d}S = \int_\Omega S\,\mathrm{d}\Omega. \tag{16}$$

The vector $\boldsymbol{W}$ contains the conservative variables.

$$\boldsymbol{W} = \{\rho, \rho u, \rho v, \rho w, \rho E, \rho k, \rho\omega\}^T, \tag{17}$$

where ρ is the density; u, v and w are the three Cartesian velocity components; and E is the specific total energy of the flow, which is given by

$$E = e + \tfrac{1}{2}(u^2 + v^2 + w^2), \tag{18}$$

where e is the internal energy. k and ω are the turbulent kinetic and specific dissipation rate, respectively.

The flux tensors $\boldsymbol{F}_c$ and $\boldsymbol{F}_d$ in equation (16) represent the inviscid convective fluxes and the diffusive fluxes, respectively. The convective fluxes $\boldsymbol{F}_c$ defined in terms of the relative velocity $u - u_b$ is

$$F_c = \begin{matrix} \rho(u-u_b) & \rho(v-v_b) & \rho(w-w_b) \\ \rho u(u-u_b)+p & \rho u(v-v_b) & \rho u(w-w_b) \\ \rho v(u-u_b) & \rho v(v-v_b)+p & \rho v(w-w_b) \\ \rho w(u-u_b) & \rho w(v-v_b) & \rho w(w-w_b)+p \\ \rho\left(E+\frac{p}{\rho}\right)u-u_b & \rho\left(E+\frac{p}{\rho}\right)(v-v_b) & \rho\left(E+\frac{p}{\rho}\right)(w-w_b) \\ \rho k\ u-u_b & \rho k(v-v_b) & \rho k(w-w_b) \\ \rho\omega\ u-u_b & \rho\omega(v-v_b) & \rho\omega(w-w_b) \end{matrix} \tag{19}$$

where $u_b = (u_b, v_b, w_b)^T$ is the grid velocity vector. The diffusive fluxes due to the viscous shear stresses, thermal diffusion and turbulence diffusion can be written as

$$F_d = \begin{matrix} 0 & 0 & 0 \\ \tau_{xx} & \tau_{xy} & \tau_{xz} \\ \tau_{yx} & \tau_{yy} & \tau_{yz} \\ \tau_{zx} & \tau_{zy} & \tau_{zz} \\ u\tau_{xx}+v\tau_{xy}+w\tau_{xz}-q_x & u\tau_{yx}+v\tau_{yy}+w\tau_{yz}-q_y & u\tau_{zx}+v\tau_{zy}+w\tau_{zz}-q_z \\ \mu*\frac{\partial k}{\partial x} & \mu*\frac{\partial k}{\partial y} & \mu*\frac{\partial k}{\partial z} \\ \mu*\frac{\partial \omega}{\partial x} & \mu*\frac{\partial \omega}{\partial y} & \mu*\frac{\partial \omega}{\partial z} \end{matrix} \tag{20}$$

where

$$\mu^* = \mu_L + \sigma^*\mu_T, \tag{21}$$

where μ_L is the laminar viscosity, μ_T is the turbulent eddy viscosity, σ^* is the turbulent closure constant equal to 0.5, and $\tau_{\alpha\beta}$ with $\alpha, \beta \in \{x, y, z\}$ is the stress tensor as shown below

$$\tau_{\alpha\beta} = \mu(\partial_\alpha u_\beta + \partial_\beta u_\alpha) - \tfrac{2}{3}\mu\delta_{\alpha\beta}\partial_\alpha u_\beta \tag{22}$$

$$q_\alpha = -k\partial_\alpha\Theta. \tag{23}$$

In the above equations, μ means the dynamic viscosity, k signifies the thermal conductivity and Θ the temperature. The stress tensor $\tau_{\alpha\beta}$ is the general form for the shear stresses in $\boldsymbol{F}_d$.

The source term $\boldsymbol{S}$ is defined as

$$S = \begin{Bmatrix} 0 \\ 0 \\ 0 \\ 0 \\ 0 \\ \tau_{\alpha\beta}\frac{\partial u_\alpha}{\partial x_\beta} - b^*\rho\omega k \\ \frac{a\omega}{k}\tau_{\alpha\beta}\frac{\partial u_\alpha}{\partial x_\beta} - b\rho\omega^2 \end{Bmatrix} \tag{24}$$

with closure constants of $a = 5/9$, $b = 0.075$ and $b^* = 0.09$.

The space discretization in the above equations is done based on a finite volume approach. The cell-centred based method is used to calculate gradients. The discretization of the convective fluxes is based on a second-order Roe's flux-difference splitting scheme for NS equations and a second-order upwind scheme for turbulent convective fluxes. The discretization of the diffusive fluxes is based on a second-order finite-differencing. To cope with the complicated moving mesh of two oscillating wings, a structured multi-block mesh is generated. Parallel computing with MPI is used to accelerate the solution procedure. The coupled RANS equations along with k-ω turbulence equations are solved with a dual time-stepping marching algorithm for unsteady flow. Detailed numerical methods can be found in papers by Xiao *et al* (2007), (2012) and Xiao and Liao (2010). Although a compressible flow solver is used for the present study, from our past studies on various incompressible flows with this solver at a very low incoming Mach number of 0.06 (Xiao and Liao 2009, 2010, Xiao *et al* 2012), the agreement between our simulation results with other experiments or modelling is excellent.

2.3. Validation

The numerical methods developed for this study have been extensively validated for a single rigid oscillating foil, either for propulsion or energy extraction (Xiao and Liao 2010, Xiao *et al* 2012). To validate the capability of the current solver to deal with the flexible models proposed herein, a study on an undulating fish model is performed and the results are compared with those of Deng *et al* (2007) in figures 4(*a*) and (*b*). The non-dimensional undulating phase speed (f_λ) is defined as

$$f_\lambda = \frac{2\pi f}{k_\lambda}, \tag{25}$$

where f is the undulation frequency and k_λ is the non-dimensional wave length. As can be seen clearly, our predicted results show a good correlation with theirs for both the drag coefficient and fluid fields.

Extensive tests on the two-equation k-ω turbulence models are performed and the results are summarized in table 2, and compared with those of Kinsey and Dumas (2012a). A typical case is a single oscillating foil with NACA0015 shape flapping at f^* of 0.14. The pitching and heave amplitude are 75° and 1.0c, and the far-stream Reynolds number equals to 5×10^5.

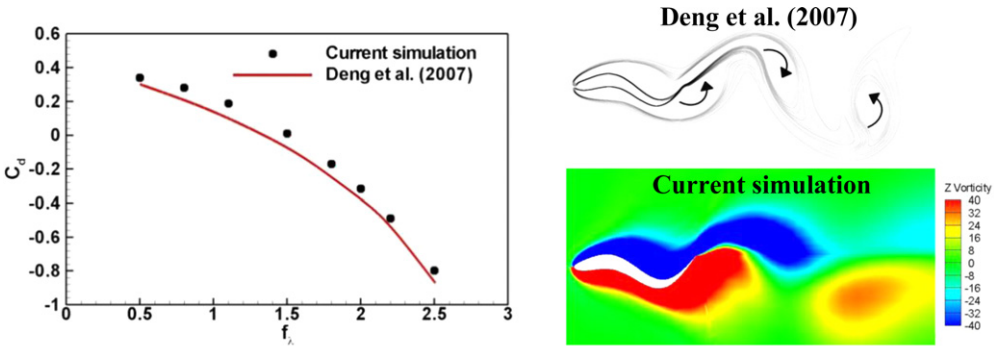

(*a*) Drag coefficient validation (*b*) Vorticity contour validation

Figure 4. Flexible model validation of (*a*) time-averaged drag coefficient (C_d) variation with f_λ, (*b*) instantaneous vorticity contour at $f_\lambda = 0.5$ and $t/T = 1/8$ (comparison with Deng *et al* (2007)).

Table 2. Turbulence k-ω model validation with Kinsey and Dumas (2012a).

Mesh	Number of time steps per period	Iterations for one pseudo time step	CFL number	C_{op}
51216	128	100	7	0.96
51216	128	200	3	0.95
51216	64	100	7	0.9
51216	64	200	3	0.89
265740	128	100	7	1.03

Current k-ω model validation (comparison with Kinsey and Dumas (2012a), $C_{op} = 0.994$) NACA0015, $Re = 5 \times 10^5$, $f^* = 0.14$, pitching amplitude $= 75°$, pitching axis $= c\ 3^{-1}$ and $h_0/c = 1$.

It is found that the final result is sensitive to a number of parameters related to the CFD solver, i.e. the number of mesh cells, the iteration time step either in physical time or pseudo time steps as well as the Courant–Friedrichs–Lewy (CFL) number. Considering the compromise between accuracy and computational time, the medium mesh (51216 cells) with 128 time steps per cycle, 100 iterations per time step and CFL of 7 is selected for our following simulations.

3. Results and discussions

3.1. Mechanism of various bio-inspired flexible shapes for a single wing

It is generally accepted that a flapping wing with some degree of flexibility can potentially provide an improved propulsion performance that is otherwise impossible for a rigid wing. The fundamental mechanisms behind this may be attributed to (1) the change of local effective AoA due to the flexible deformation of the wing shape; and (2) the enhanced stability of LEV shedding (Zhu 2007, Nakata and Liu 2012). The present study will show that a flexible wing can generate much more power than a rigid wing even when the wing is merely flapping for energy extraction. The local effective AoA and the stability of LEV also influence the efficiency of the energy extraction situation, the mechanism of which is more or less similar to the propulsion situations.

Figures 5(*a*) and (*b*) display the mean power coefficient and efficiency for four models at two heave amplitudes (h_0/c)

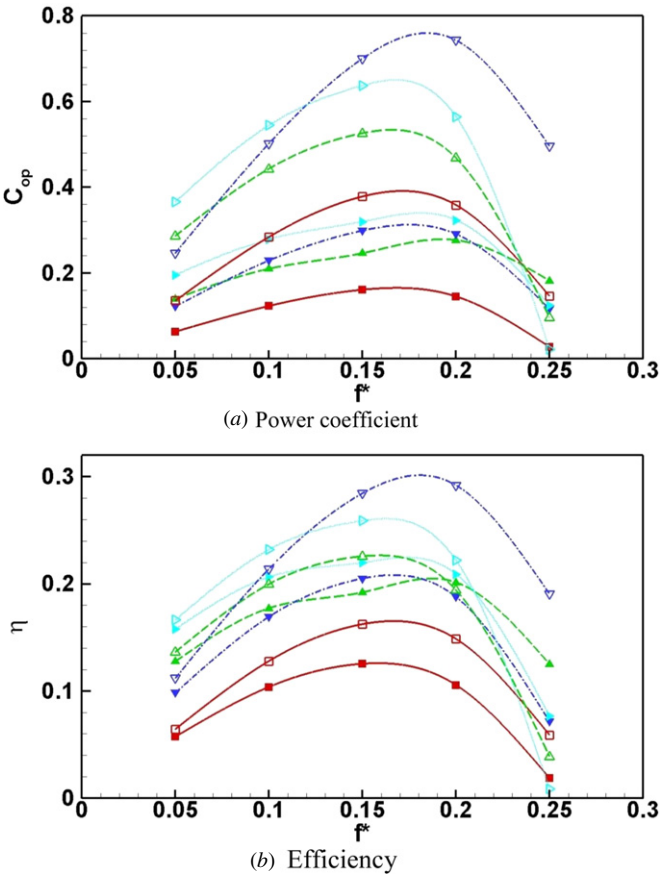

(*a*) Power coefficient

(*b*) Efficiency

Figure 5. Comparison of (*a*) power coefficient and (*b*) efficiency among various flexible/rigid modes with nominal effective AoA of 10°. ($h_0/c = 0.5$ ■: rigid, ▲: LEC, ▼: TEC and ►: integrated) and ($h_0/c = 1.0$ □: rigid, Δ: LEC, ∇: TEC and ▷: integrated); $\alpha_f =$ 30°(LEC) and $d_b/c = 0.15$ (TEC) and $\alpha_f = 30°$ plus $d_b/c = 0.15$ (integrated model).

of 0.5 and 1.0 with nominal effective AoA of 10°. As can be clearly seen from the figures, within the f^* from 0.05 to 0.25, all flexible flapping wings generate larger efficiency than the rigid wing. Given $f^* = 0.15$, the efficiency is increased from 12.5% (rigid) to 21.9% (integrated model) for $h_0/c = 0.5$ and from 16.2% (rigid) to 28.4% (TEC) for $h_0/c = 1.0$, respectively. The improvement is especially profound when the wing flaps at small heave amplitude. However, the best flexible morphography is reliant on the particular

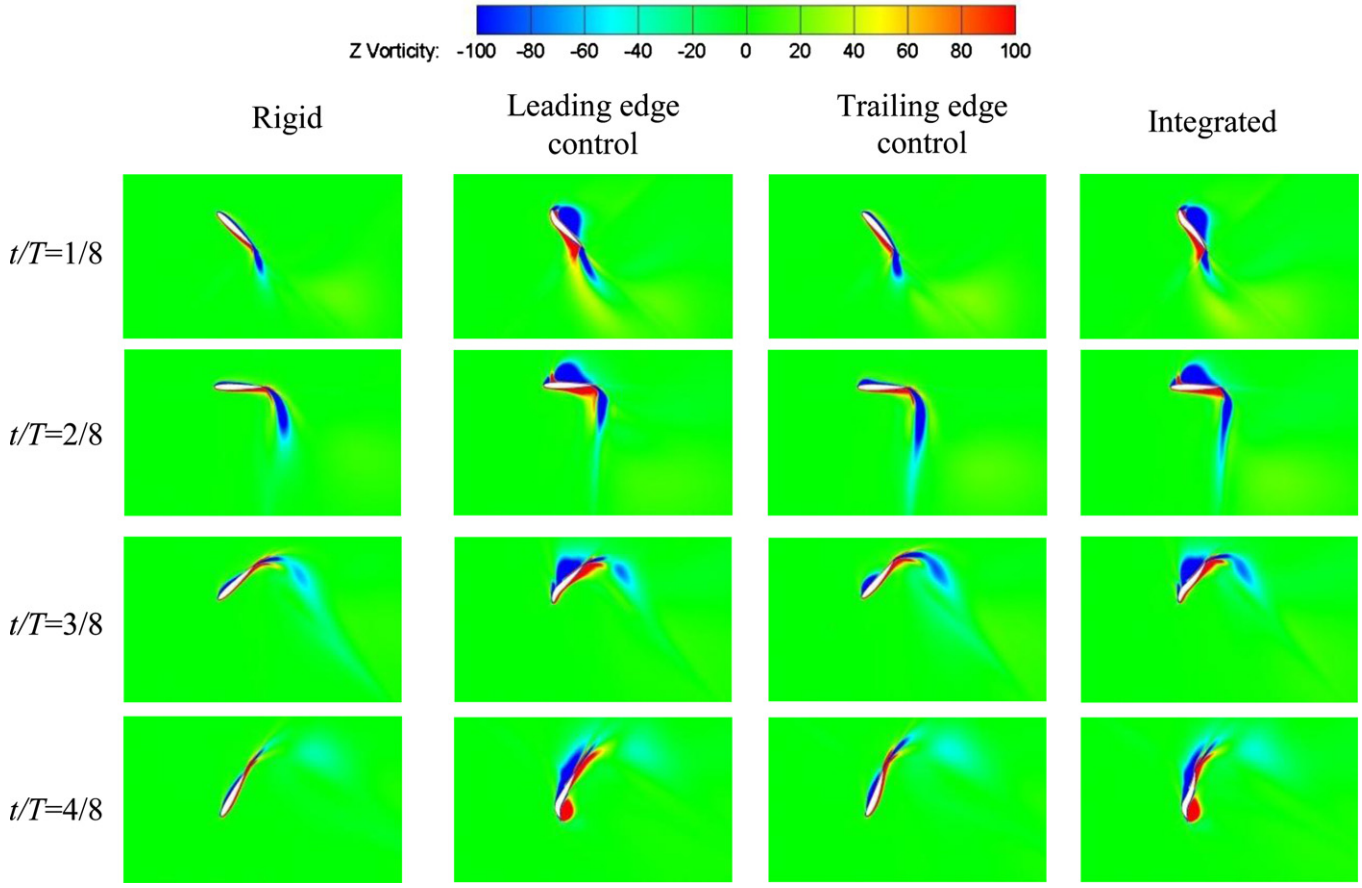

Figure 6. Instantaneous vortex contours over half a cycle for various flexible/rigid wings $h_0/c = 1.0$; $f^* = 0.2$; nominal effective AoA of 10°; $\alpha_f = 30°$ (LEC) and $d_b/c = 0.15$ (TEC) and $\alpha_f = 30°$ plus $d_b/c = 0.15$ (integrated model).

flapping parameters, such as flapping frequency, pitch and heave amplitude, flexible coefficient, local leading/trailing edge displacement or more specifically the nominal and local effective AoA a_0 and $(a_l(t, x))$, which we will discuss shortly.

In order to examine the influence of wing flexibility on its performance, we begin our investigation on the behaviour of a rigid wing. The evolution of LEV is depicted in figure 6 over half a cycle. It can be seen that at instantaneous time $t/T = 1/8$ the LEV starts to generate and further develops at $t/T = 2/8$. At $t/T = 3/8$, the wing undergoes its downstroke motion, the LEV sheds from the LE, convects to the wing trailing edge and eventually sheds into wake, leaving behind a shear layer near its trailing edge at $t/T = 4/8$. The above general observation is consistent with our early investigation (Xiao *et al* 2012), Kinsey and Dumas (2008) and the results of Peng and Zhu (2009). Previous studies on the rigid wing device indicated that the LEV plays a leading role in the device power generation enhancement by increasing the instantaneous lifting force and moment coefficient (Peng and Zhu 2009, Xiao *et al* 2012). Flapping wing devices could generate and maintain LEV because of the pressure gradient and non-inertial forces during their downstroke motion. The LEV could generate a low pressure region compared with the surrounding fluid field. Such a low pressure region produces a suction effect on the upper surface of the flapping wing which could enlarge the pressure difference between the upper and lower surface and result in an enhancement on the lift amplitude during the flapping period (Shyy and Liu 2007). The LEV could be attached to the wing surface during the whole downstroke motion which acts like an energy resource to provide extra lift to the device continuously. A high efficiency is obtained when the energy of LEV is 'recovered' by the wing. This is also well manifested by the instantaneous C_l and C_m plot in figure 7. As LEV starts to generate and develop, the peak lift force (C_l) increases and the moment (C_m) remains at a high value. Once the LEV fully develops and sheds from the LE, the C_l reaches its highest value, and both C_l and C_m decrease afterwards.

Apart from the instantaneous magnitude of C_l and C_m, with regard to device power or efficiency (as depicted by equation (14)), it is also influenced by the phase shift between C_l and heaving velocity ($\mathrm{d}h/\mathrm{d}t$) as well as C_m and pitching angular velocity ($\mathrm{d}\theta/\mathrm{d}t$) (Xiao *et al* 2012, Kinsey and Dumas 2008). Since the power is the product of force multiplied by the displacement velocity, to achieve high power efficiency, both C_m and $\mathrm{d}\theta/\mathrm{d}t$ are expected to co-exist in the same sign over one cycle.

Figures 7(*a*) and (*b*) show the comparison of time distribution of C_l, $\mathrm{d}h/\mathrm{d}t$, C_m and $\mathrm{d}\theta/\mathrm{d}t$ for four models. Given a rigid wing, a near-sinusoidal profile presents for the above four parameters, which further leads to a similar trend of instantaneous $C_{op,}$ as shown in figure 8. The phase shift between C_l and $\mathrm{d}h/\mathrm{d}t$ is $\pi/3$ approximately, which allows the C_l and $\mathrm{d}h/\mathrm{d}t$ to have the same sign over more than half of the cycle, leading to a positive contribution from $C_l \times \mathrm{d}h/\mathrm{d}t$ to

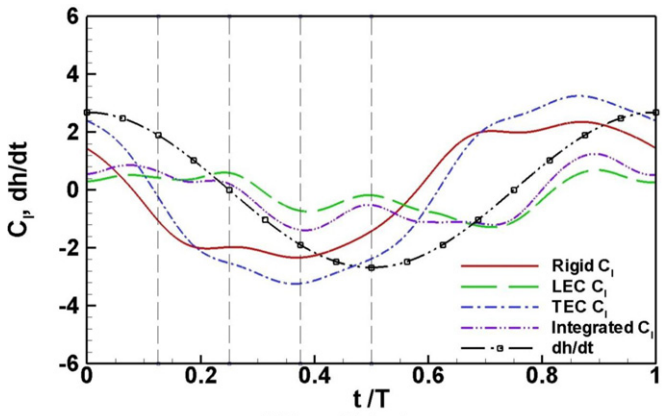

(*a*) Lift coefficient

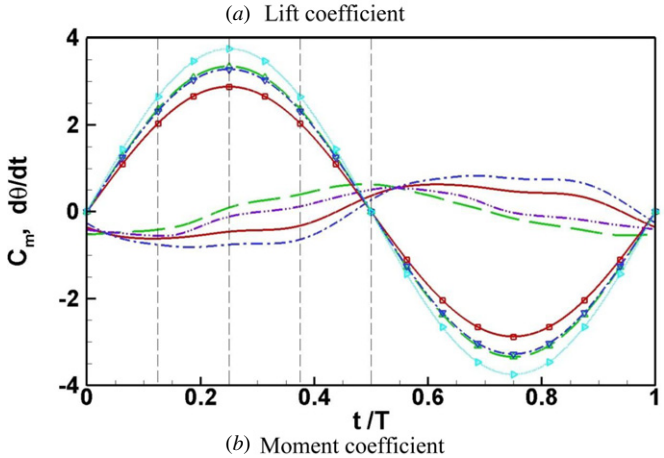

(*b*) Moment coefficient

Figure 7. Instantaneous lift coefficient and moment coefficient (*a*) lift coefficient, (*b*) moment coefficient $h_0/c = 1.0$; $f^* = 0.2$; nominal effective AoA of 10°; $\alpha_f = 30°$ (LEC) and $d_b/c = 0.15$ (TEC) and $\alpha_f = 30°$ plus $d_b/c = 0.15$ (integrated model). In (*b*), solid line: rigid C_m, dashed line: LEC C_m, dash dot line: TEC C_m, dash double dot line: integrated C_m, ■: rigid $\mathrm{d}\theta/\mathrm{d}t$, ▲: LEC $\mathrm{d}\theta/\mathrm{d}t$, ▽: TEC $\mathrm{d}\theta/\mathrm{d}t$ and ▷: integrated $\mathrm{d}\theta/\mathrm{d}t$.

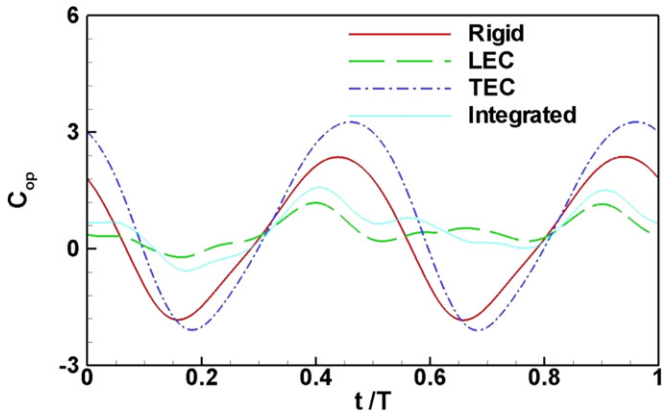

Figure 8. Instantaneous power coefficient with nominal effective AoA of 10° and $h_0/c = 1.0$; $f^* = 0.2$. For a flexible wing $\alpha_f = 30°$ (LEC) and $d_b/c = 0.15$ (TEC) and $\alpha_f = 30°$ plus $d_b/c = 0.15$ (integrated model).

the mean power output. However, the phase shift between C_m and $\mathrm{d}\theta/\mathrm{d}t$ is nearly π, as displayed in figure 7(*b*), and thus in this case they will result in opposite signs, giving a negative contribution from $C_m \times \mathrm{d}\theta/\mathrm{d}t$ to the mean power.

A different phase shift scenario appears when the wing is modelled with the LEC shape. As seen in figures 7(*a*) and (*b*), for the majority of the time throughout a cycle, the C_l and $\mathrm{d}h/\mathrm{d}t$ for the LEC model present the same sign. The phase shift between C_m and $\mathrm{d}\theta/\mathrm{d}t$ reduces to $\pi/2$, resulting in a positive contribution from $C_m \times \mathrm{d}\theta/\mathrm{d}t$ to the mean power output. The above force-velocity relation aligns with the different LEV interaction modes for rigid and LEC flapping wing, as depicted in figure 6. At $t/T = 1/8$, where the wing pitches to its maximum angle, the LEV of LEC fully develops and sheds from LE at $t/T = 2/8$, which is much earlier than for a rigid wing. In addition, the LEV of LEC is larger than that of a rigid wing, forming a large separation region near the trailing edge when the LEV reaches the wing trailing edge. The peak values of the lift coefficient are influenced by both the size/strength of LEV at the LE and the flow separation region near the trailing edge. Recall that the mechanism of LEV provides a low-pressure region to supply extra lift to the wing. A larger size/strength of LEV results in a large area/lower pressure for the low-pressure region which could supply more lift to the wing. The superposition result of the above two effects can be seen in figures 7 and 8, where the lift coefficient distribution gives multiple peaks but a smaller amplitude, in comparison to its rigid wing counterpart.

With the case of TEC, as displayed in figures 7 and 8, the trends of C_l, $\mathrm{d}h/\mathrm{d}t$, C_m, $\mathrm{d}\theta/\mathrm{d}t$ and C_{op} are essentially the same as those of a rigid wing. However, the peak values of the lift coefficient significantly increase from 2.35 of a rigid wing to 3.25 for TEC, and a remarkable increase in C_{op} can also be observed from figure 8, leading to enhanced mean power efficiency. This is attributed to the enlarged LEV strength for TEC in comparison to a rigid wing, as depicted in figure 6.

With the results presented above we can make the following general observations about a flexible wing with a LEC and TEC model. Generally, a wing of LEC shape, where the wing deforms easily at the LE, can trigger the LEV to develop at an earlier stage than a rigid wing. As a consequence, the phase-shift between (C_l and $\mathrm{d}h/\mathrm{d}t$) and (C_m and $\mathrm{d}\theta/\mathrm{d}t$) can present a favourable trend to enhance the cycle-mean power. On the other hand, a flexible wing of TEC shape, where the main deformation occurs near the trailing edge, can enhance the size and strength of LEV and thus increase the total power via increasing the peaks of lift and moment coefficients. It is expected that an even better performance can be achieved by employing both a flexible wing with an appropriately designed combination of LEC and TEC shapes. Our results for an integrated model clearly prove the above hypothesis, as shown in figures 5–8.

Specific attention is drawn to the role of effective AoA on the power. Figures 9(*a*)–(*c*) shows the local AoA distribution along the chord-wise direction at an instantaneous time of $t/T = 1/8$, when the wing pitches to its maximum amplitude, i.e. $\theta_t(t) = \theta_0$. As can be clearly seen from the figures, although the nominal effective AoA $\alpha_0 = 10°$ is identical for all four models, the local effective AoA ($\alpha_t(t, x)$) varies significantly with various models, as does the degree of the overall flexible deformation (represented by n), and local stiffness at leading and trailing edge (α_f and d_b). In particular, the flexible wing displays a large $\alpha_t(t,x)$ in comparison to a rigid wing at the same chord-wise location, which as a consequence leads to

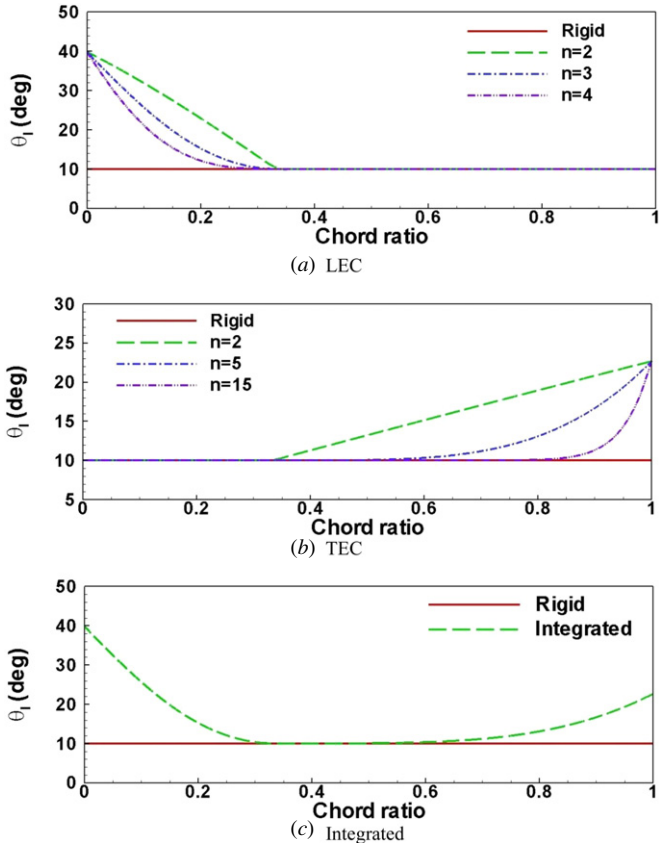

Figure 9. Foil local AoA along chord-wise direction at $\theta_l(t) = \theta_0$ for different flexible coefficients (n) at nominal effective AoA $\alpha_0 = 10^\circ$. (a) LEC, $\alpha_f = 30^\circ$. (b) TEC, $d_b/c = 0.15$. (c) Integrated model $\alpha_f = 30^\circ$ and $d_b/c = 0.15$.

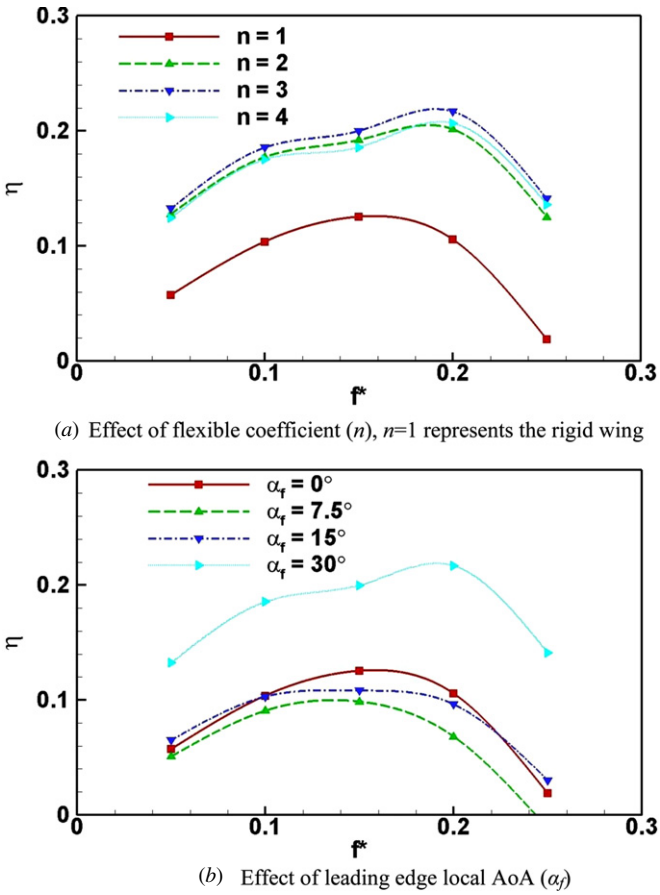

Figure 10. Various LEC parameters' effect on the cycle-mean efficiency at nominal effective AoA $\alpha_0 = 10^\circ$. (a) Flexible coefficient (n), (b) leading edge local AoA α_f ($h_0/c = 0.5$).

the different behaviour of LEV, the lift and moment coefficient and then the efficiency.

In the following sections our investigations will be focused on a systematic parametric study to examine other relevant flexible influences on power efficiency.

3.2. Parametric study

3.2.1. Leading edge control model. The main cases simulated in this section are provided in table 1. These include the effect of flexible coefficient (n) and local LE AoA (α_f). As mentioned earlier, the flexible coefficient is an indication of wing flexibility along the chord-length direction. On the other hand, the local LE AoA (α_f) presents the potential for local deformation at the wing LE.

Flexible coefficient (n). As shown in figures 9(a)–(c) and equation (4), the flexible coefficient n determines the degree of flexibility of a wing in the chord-wise direction. The cases studied are associated with n of 1, 2, 3 and 4, where n equals to 1 indicating a rigid wing. The influence of the flexible coefficient on the cycle-mean efficiency is shown in figure 10(a). For all cases studied here, though a flexible wing is better than a rigid wing, as was discussed in the last section, the best performance is achievable if the wing shape deforms moderately, particularly the case of n being 3.0. The instantaneous C_l and C_m distribution displayed in figure 11(a) reveals that while the flexible coefficient has no impact on the phase shift of (C_l~dh/dt) and (C_m~dθ/dt), it influences the peak values of C_l and C_m. Specifically, at a large n, C_l amplitude increases while C_m decreases. Recall a negative effect from ($C_m \times$ dθ/dt) to mean power; a lessened peak C_m is beneficial to improve power.

Local leading edge AoA (α_f). The influence of local LE AoA has been investigated with α_f of 7.5°, 15° and 30°. As shown in figure 10(b), where the time-mean efficiency is plotted for various local LE AoAs, a deteriorated effect on the power is depicted at low α_f. However, by increasing α_f to a large value, the efficiency is profoundly increased in comparison to a rigid wing ($\alpha_f = 0^\circ$). Figure 11(b) shows the instantaneous distribution of C_l and C_m for different α_f. The impact of α_f on power is established via its influence on peak values of C_l and C_m as well as the phase shifting between C_l and dh/dt, and C_m with dθ/dt. Increasing α_f to a critical value ($\alpha_f \geqslant 15^\circ$) leads to a profoundly enlarged C_l, and a reduced phase shift between C_m and dθ/dt, from π to $\pi\ 2^{-1}$ corresponding to a rigid and LEC. This is consistent with the LEV effect associated with a flexible LEC, as discussed in the section 3.1.

3.2.2. Trailing edge control model. With this model there are two parameters influencing the power, which are flexible coefficient (n) and trailing edge displacement (d_b), as defined in

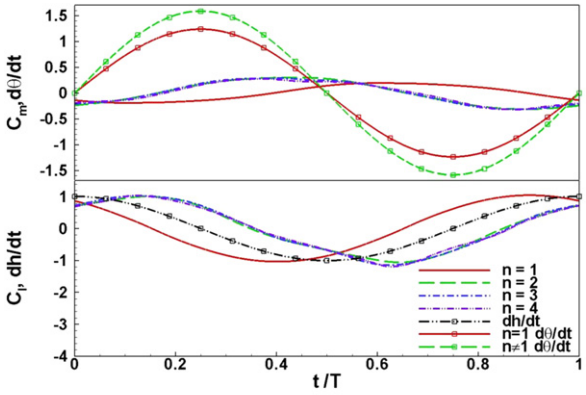

(*a*) *n* effect on C_l, *dh/dt*, C_m and *dθ/dt*

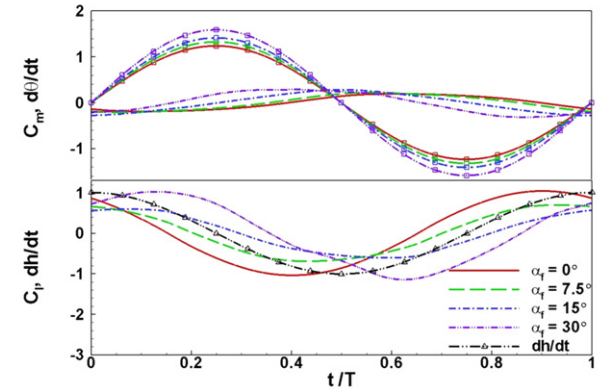

(*b*) α_f effect on C_l, *dh/dt*, C_m and *dθ/dt*. □ with line: corresponding *dθ/dt*.

Figure 11. Instantaneous C_l, d*h*/d*t*, C_m and dθ/d*t* (LEC $h_0/c = 0.5$; $f^* = 0.15$) at nominal effective AoA $\alpha_0 = 10^\circ$. (*a*) Flexible coefficient effect and (*b*) α_f effect.

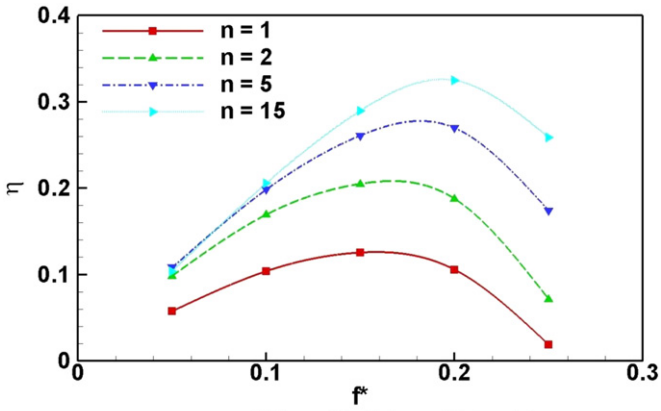

(*a*) Effect of flexible coefficient (*n*)

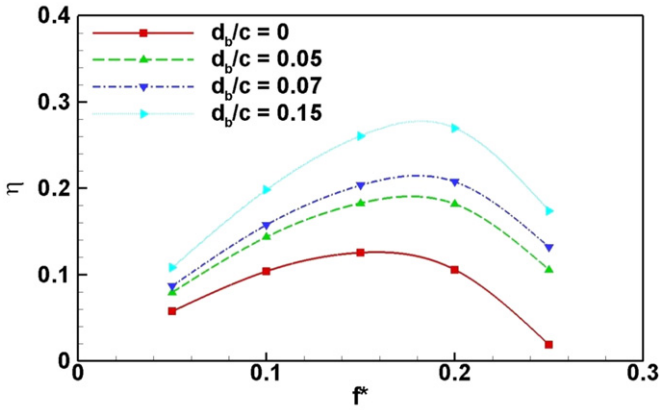

(*b*) Effect of trailing edge displacement d_b

Figure 12. Effect of TEC parameters on the time-mean efficiency at nominal effective AoA $\alpha_0 = 10^\circ$. (*a*) Flexible coefficient (*n*) and (*b*) trailing edge displacement (d_b/c) ($h_0/c = 0.5$).

equation (4). In this section, the effects of these two parameters are investigated.

Flexible coefficient (n). Three different flexible coefficients of 2, 5 and 15 are studied in this section. Distinguishing from the little *n* effect on an LEC model, it has a remarkable influence on the power efficiency of the TEC model, principally on the large flapping frequency. As can be seen from the cycle-mean efficiency in figure 12(*a*), the addition of flexibility to a TEC monotonically improves the power with flexible coefficient *n*. Also, the peak efficiency even occurs at a larger f^* of 0.2, as compared to $f^* = 0.15$ for a rigid wing. A detailed analysis of the instantaneous C_l and C_m plot is shown in figure 13(*a*). As can be seen from the plot, large *n* results in a significant increase in C_l amplitude. However, although the higher efficiency can be achieved by increasing the flexible coefficient, considering a reasonable stiffness of biological animals in nature, the largest *n* of 15 in the present study is not recommended when this conceptual design is applied to the industry device. Instead, a moderated *n* of 5 is highly recommended.

Trailing edge displacement (d_b/c). Figure 12(*b*) shows the time-averaged efficiency for the trailing edge displacement effect on the TEC model. It is evident that a large displacement near the trailing edge can help to enhance the energy extraction in comparison to a rigid model with zero deformation at TE. A significant improvement can be seen for the frequency (f^*) between 0.1 and 0.2. The general trend of instantaneous C_l and C_m curve shown in figure 13(*b*) is very similar to that of the flexible coefficient *n* effect. The peak values of C_l and C_m have been continuously increasing with the increasing of trailing edge displacement. Moreover, although the pitching velocity (dθ/d*t*) slightly increases at a large d_b/c, which is expected to detriment the mean-power by increasing the negative contribution from ($C_m \times$ dθ/d*t*), the improvement in the net cycle-mean power is still remarkable because of the profound increase of C_l.

3.3. Integrated model

As mentioned earlier, an integrated flexible wing is expected to gain a larger efficiency than a LEC and TEC. The study on an integrated model is carried out with three typical nominal effective AoA of 0°, 5° and 10°. The results of mean efficiency against flapping frequency are shown in figure 14. As can be seen clearly, with all three effective AoAs being examined, an enhanced efficiency is observable with the use of a flexible integrated model and this behaviour becomes more remarkable at low effective AoA. For example, at $\alpha_0 = 10^\circ$, the peak efficiency increases from 12.5% of the rigid wing to 22.1% of the flexible integrated wing, while at $\alpha_0 = 0^\circ$, η increases from 1.9% to 13.6%.

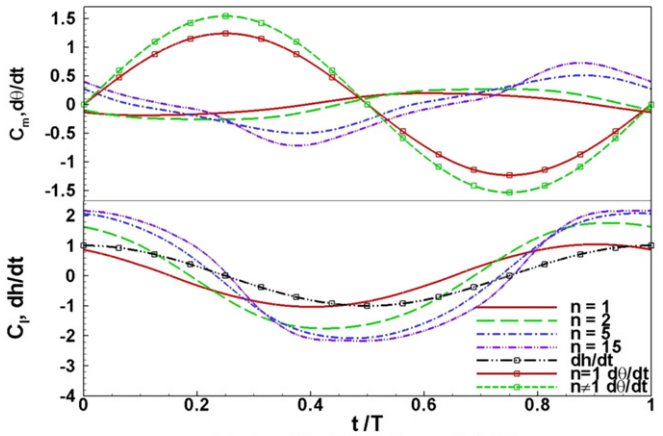

(*a*) *n effect on* C_l, *dh/dt,* C_m *and* $d\theta/dt$

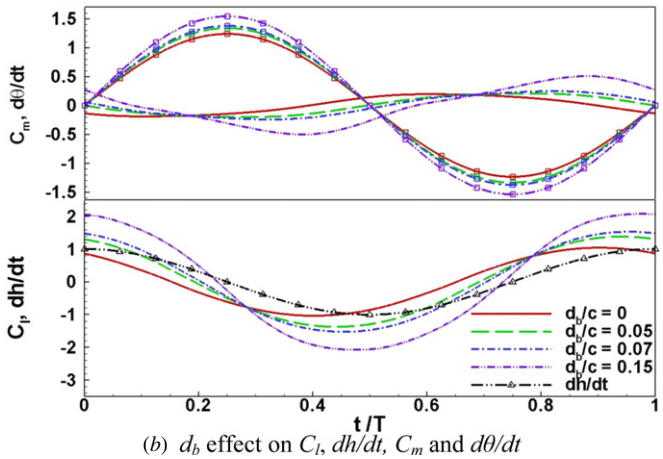

(*b*) d_b effect on C_l, dh/dt, C_m and $d\theta/dt$

Figure 13. Instantaneous C_l, d*h*/d*t*, C_m and dθ/d*t* (TEC with $h_0/c = 0.5$; $f^* = 0.15$) at nominal effective AoA $\alpha_0 = 10^\circ$. (*a*) Flexible coefficient effect and (*b*) trailing edge deformation effect. Open square with lines: dθ/d*t*.

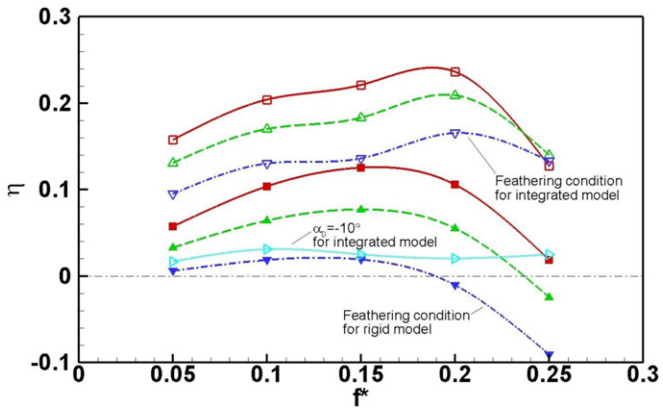

Figure 14. Comparison of time-mean efficiency versus f^* between integrated flexible wing and a rigid wing for various α_0 (■: rigid $\alpha_0 = 10^\circ$, ▲: rigid $\alpha_0 = 5^\circ$, ▼: rigid $\alpha_0 = 0^\circ$, □: integrated $\alpha_0 = 10^\circ$, **Δ**: integrated $\alpha_0 = 5^\circ$, ∇: integrated $\alpha_0 = 0^\circ$ and □: integrated $\alpha_0 = -10^\circ$) with $h_0/c = 0.5$; $\alpha_f = 30^\circ$; $d_b/c = 0.15$; $n = 3$ for leading edge and $n = 5$ for trailing edge.

Special attention is paid to the case with a nominal effective AoA of zero ($\alpha_0 = 0^\circ$), i.e. the feathering condition. A totally diverse feathering behaviour is shown in figure 14 for a rigid and flexible wing. At $\alpha_0 = 0^\circ$, the efficiency of

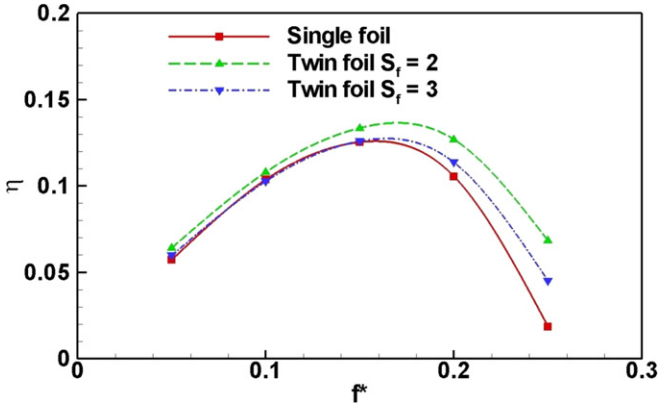

Figure 15. Comparison of time-mean efficiency versus f^* under twin rigid foils configuration for different gap ratio with $h_0/c = 0.5$ at nominal effective AoA $\alpha_0 = 10^\circ$.

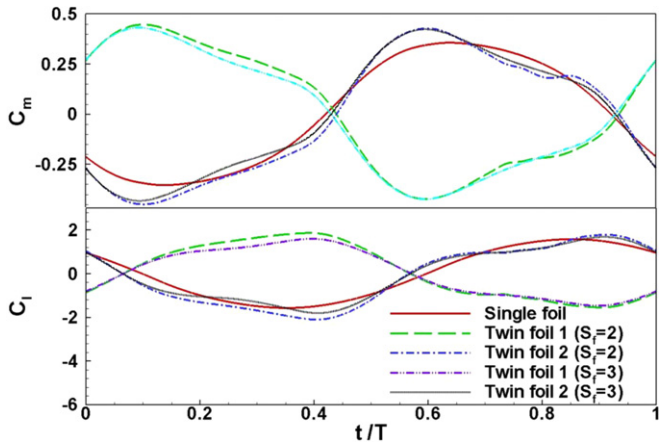

Figure 16. Instantaneous lift coefficient and moment coefficient for rigid single and twin foil at nominal effective AoA $\alpha_0 = 10^\circ$ with $h_0/c = 0.5$ and $f^* = 0.2$.

a rigid wing is more or less zero, which is consistent with the feathering definition (Kinsey and Dumas 2008). However, with the use of a flexible integrated model, the wing operates in the power generation regime with the maximum efficiency of 10%. The actual feathering condition for a flexible integrated model, indicated by a zero mean efficiency, is reduced to a nominal effective AoA of -10°.

3.4. Parallel twin wing

The parallel twin-wing configuration is studied with the aim of examining whether a biomimetic concept of animals moving as a group can be similarly applied to energy devices. The study of rigid and TEC models is carried out with different gap ratios and nominal effective AoA of 0°, 5° and 10°.

3.4.1. Gap ratio (S_f). The comparison between a rigid single wing and parallel twin wings is shown in figure 15 with heaving amplitude h_0 of $0.5c$ and α_0 equivalent to 10°. Generally, a parallel twin-foil configuration improves the efficiency in comparison to a single wing, especially at a large flapping frequency. A small gap between two wings is beneficial to enhance the overall efficiency. The instantaneous distribution of lift and moment coefficients displayed in figure 16 at

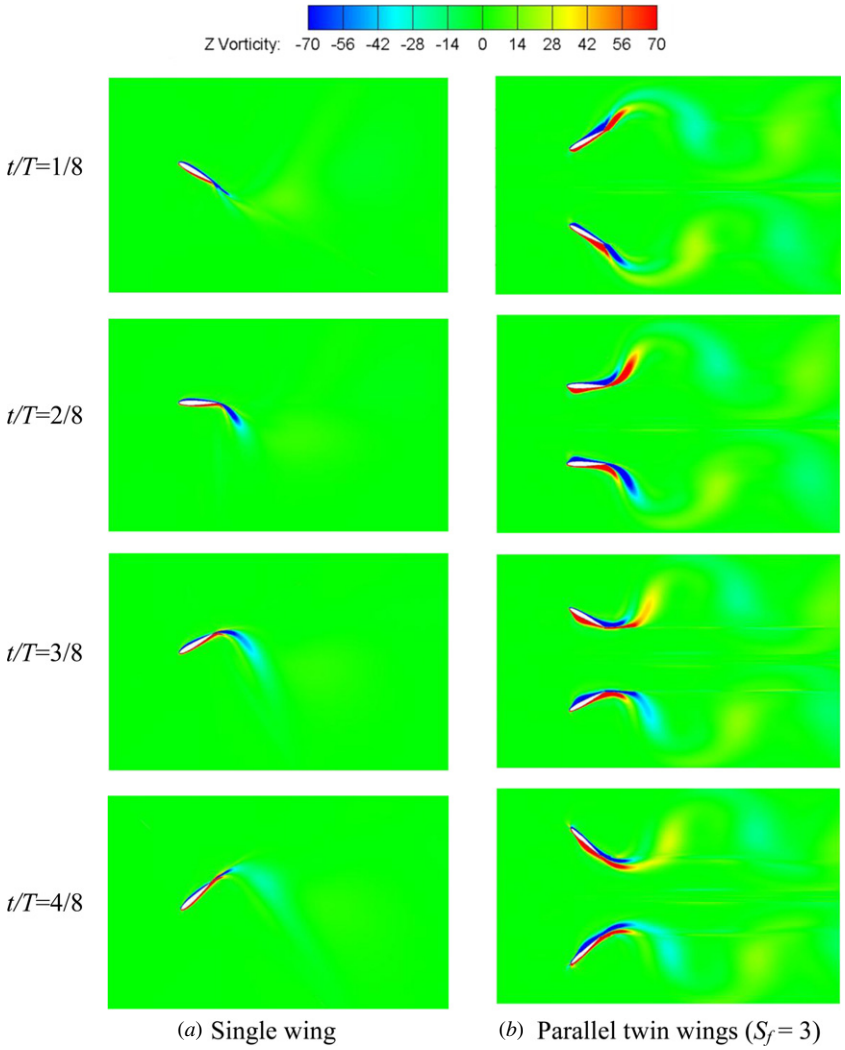

Figure 17. Comparison of instantaneous vortex contours at nominal effective AoA $\alpha_0 = 10^\circ$ for (*a*) single rigid wing and (*b*) parallel rigid twin wings ($S_f = 3$) with $h_0/c = 0.5$; $\alpha_0 = 10^\circ$ and $f^* = 0.2$.

$f^* = 0.2$ reveals a slightly enlarged amplitude of C_l and C_m. With the analysis of the comparison of a single and twin wings for instantaneous vortex contour, as shown in figure 17, a stronger vortex interaction is observed around twin wings than a single wing, which is believed to be the cause for the improved power. The behaviour observed here very much resembles the schooling fish and flying insects in nature, when they move from one place to another in order to preserve their propulsion energy. The present results also indicate that a parallel arranged twin wing can generate more power than a single wing with a similar biological mechanism.

3.4.2. Nominal effective AoA (α_0). The time-mean efficiency against the flapping frequency with different α_0 is shown in figure 18. A similar phenomenon can be found when a single flexible wing model is observed, e.g. by applying a flexible TEC with a small α_0 ($\alpha_0 = 0^\circ$ and 5°), and a larger efficiency is achieved especially at a large flapping frequency. However, the efficiency reduces with $\alpha_0 = 10^\circ$ at a large flapping frequency. An examination of the detailed flow structure shows that too large an AoA destroys the benefits from a favourable vortex interaction between twin wings.

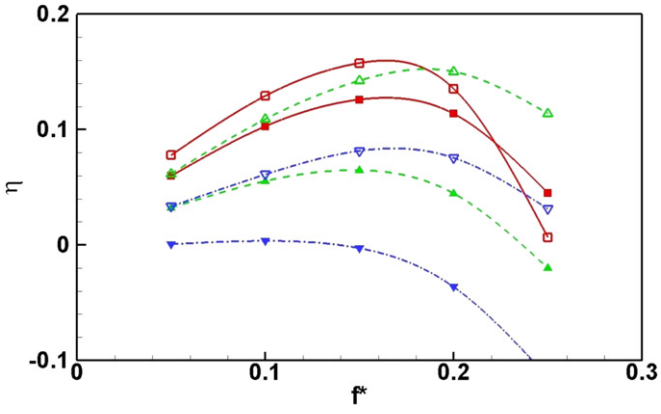

Figure 18. Comparison of time-mean efficiency versus f^* under twin-wing configuration (TEC model ($d_b/c = 0.05$) versus rigid model with $h_0/c = 0.5$ and $S_f = 3$). ■: rigid, $\alpha_0 = 10^\circ$, △: rigid, $\alpha_0 = 5^\circ$, ▽: rigid, $\alpha_0 = 0^\circ$; □: TEC, $\alpha_0 = 10^\circ$, **▲**: TEC, $\alpha_0 = 5^\circ$, ∇: TEC, $\alpha_0 = 0^\circ$.

4. Conclusions

We have performed a turbulent CFD simulation of an ocean tidal energy extraction device consisting of an oscillating/flapping flexible single and twin wing. The concept is inspired by the flexible wings of natural flying insects/birds and swimming fish. Particularly, the LEC, TEC and a further developed integrated model combining the best features of the above two models.

The simulation shows that the chord-wise deformation causes a remarkable increase in the local AoA, leading to the enhanced power efficiency of a flexible wing device compared to a rigid wing. The hydrodynamic performance of the wing is affected not only by the increased instantaneous lift and moment amplitude due to the deformation, but also by the phase shift among lift and heaving-velocity and moment and pitching-velocity, by initiating an earlier development of LEV. The contribution from the peak force and phase shift to the overall cycle-mean power efficiency very much depends on the specific models, i.e. whether the deformation mainly occurs in the vicinity of the trailing edge like a hawkmoth wing or near the LE as with a trout ray fin, as well as the degree of flexibility. Our systematic simulation results find that, with the new proposed integrated model, the power efficiency reaches a 7.68% enhancement relative to a rigid wing, which is associated with a nominal effective AoA of 10° at $f^* = 0.15$. A dramatic increase of efficiency (about six times that of a rigid wing) is obtained for a nominal effective AoA at 0°. One striking finding is that, with such a flexible wing, the pitching amplitude can be profoundly reduced when the wing operates at a feathering condition.

Studies on a parallel-arranged twin-wing configuration for various nominal effective AoAs show that twin wings generate much more power than a single wing. A relatively small gap between the two wings ($S_f = 2.0$) enriches the vortex interaction between the gap, and thus improves the energy extraction ability.

Finally, in the present study the flexible structure of wings is predetermined. In reality, insects and fish with different wing/fin stiffness and mass ratios could achieve their best performance by passive deformation. Performing a fully coupled FSI analysis to account for wing passive torsion and bending will be our next task in the future. However, it is reasonable to believe that the present work will produce a similar behaviour if we allow wing structural dynamic properties to be determined beforehand. In that case, the results of the present study could provide vital guidance for industry design on similar flapping wing energy devices.

5. Acknowledgments

The authors wish to thank Lloyd's Register Group Limited for providing partial financial support for this research. We are also grateful to the High Performance Computing (HPC) at the University of Strathclyde for their support of this work. The views expressed here are those of the authors and do not necessarily represent the policy or the views of the affiliated organizations.

References

Anderson J M, Streitlien K, Barrett D S and Triantafyllou M S 1998 Oscillating foils of high propulsive efficiency *J. Fluid Mech.* **360** 41–72

Combes S A and Daniel T L 2003a Flexural stiffness in insect wings I. Scaling and the influence of wing venation *J. Exp. Biol.* **206** 2979–87

Combes S A and Daniel T L 2003b Flexural stiffness in insect wings II. Spatial distribution and dynamic wing bending *J. Exp. Biol.* **206** 2989–97

Deng J, Shao X M and Yu Z S 2007 Hydrodynamic studies on two traveling wavy foils in tandem arrangement *Phys. Fluids* **19** 113104

Fish F E and Lauder G V 2006 Passive and active flow control by swimming fishes and mammals *Annu. Rev. Fluid Mech.* **38** 193–224

Jones K D, Lindsey K and Platzer M F 2003 An investigation of the fluid-structure interaction in an oscillating-wing micro-hydropower generator *Fluid Structure Interaction II* (Southampton: WIT Press) pp 73–82

Jones K D and Platzer M F 1997 Numerical computation of flapping-wing propulsion and power extraction *AIAA Meeting Papers* 97-0826

Kinsey T and Dumas G 2008 Parametric study of an oscillating airfoil in a power-extraction regime *AIAA J.* **46** 1318–30

Kinsey T and Dumas G 2012a Computational fluid dynamics analysis of a hydrokinetic turbine based on oscillating hydrofoils *J. Fluids Eng.* **134** 021104

Kinsey T and Dumas G 2012b Optimal tandem configuration for oscillating-foils hydrokinetic turbine *J. Fluids Eng.* **134** 031103

Lachenal X, Daynes S and Weaver P M 2012 Review of morphing concepts and materials for wind turbine blade applications *Wind Energy* **16** 283–307

Liao J C 2007 A review of fish swimming mechanics and behaviour in altered flows *Phil. Trans. R. Soc.* B **362** 1973–93

Liu H 2005 Simulation-based biological fluid dynamics in animal locomotion *Appl. Mech. Rev.* **58** 269–82

McKinney W and DeLaurier J 1981 The wingmill: an oscillating-wing windmill *J. Energy* **5** 109–15

Nakata T and Liu H 2012 Aerodynamic performance of a hovering hawkmoth with flexible wings: a computational approach *Proc. R. Soc.* B **279** 722–31

Peng Z and Zhu Q 2009 Energy harvesting through flow-induced oscillations of a foil *Phys. Fluids* **21** 123602

Sfakiotakis M, Lane D M and Davies J B C 1999 Review of fish swimming modes for aquatic locomotion *IEEE J. Ocean. Eng.* **24** 237–52

Shoele K and Zhu Q 2012 Leading edge strengthening and the propulsion performance of flexible ray fins *J. Fluid Mech.* **693** 402–32

Shyy W and Liu H 2007 Flapping wings and aerodynamic lift: the role of leading-edge vortices *AIAA J.* **45** 2817–9

Triantafyllou M S, Techet A H and Hover F S 2004 Review of experimental work in biomimetic foils *IEEE J. Ocean. Eng.* **29** 585–94

Turnock S R, Keane A J, Bressloff N W, Nicholls-Lee R F and Boyd S W 2009 Morphing of 'flying' shapes for autonomous underwater and aerial vehicles *NATO-RTO Modelling & Simulation Conf. (23–25 June, Lisbon, Portugal)* pp 1–19

Wootton R J 1990 The mechanical design of insect wings *Sci. Am.* **263** 114–20

Xiao Q and Liao W 2009 Numerical study of asymmetric effect on a pitching foil *Int. J. Mod. Phys.* C **20** 1663–80

Xiao Q and Liao W 2010 Numerical investigation of angle of attack profile on propulsion performance of an oscillating foil *Comput. Fluids* **39** 1366–80

Xiao Q, Liao W, Yang S and Peng Y 2012 How motion trajectory affects energy extraction performance of a biomimic energy

generator with an oscillating foil? *Renew. Energy* **37** 61–75

Xiao Q, Tsai H M and Papamoschou D 2007 Numerical investigation of supersonic nozzle flow separation *AIAA J.* **45** 532

Zhu Q 2007 Numerical simulation of a flapping foil with chordwise or spanwise flexibility *AIAA J.* **45** 2448–57

Zhu Q 2011 Optimal frequency for flow energy harvesting of a flapping foil *J. Fluid Mech.* **675** 495–517

Zhu Q, Haase M and Wu C H 2009 Modeling the capacity of a novel flow-energy harvester *Appl. Math. Modelling* **33** 2207–17

Zhu Q and Peng Z 2009 Mode coupling and flow energy harvesting by a flapping foil *Phys. Fluids* **21** 033601